ACS OMEGA

http://pubs.acs.org/journal/acsodf

Article

Two-Dimensional Janus Antimony Selenium Telluride with Large Rashba Spin Splitting and High Electron Mobility

Lei Zhang, Yuantong Gu, and Aijun Du*

Cite This: *ACS Omega* 2021, 6, 31919−31925

Read Online

ACCESS | Metrics & More | Article Recommendations | Supporting Information

ABSTRACT: Janus two-dimensional materials with large Rashba spin splitting and high electron mobility are rarely reported but highly desired for nanoscale spintronics. Herein, using density functional theory calculations, we predicated Janus $Sb_2Se_xTe_{3-x}$ (x = 1 or 2) monolayers simultaneously harboring these fascinating properties. The predicated monolayers are indirect semiconductors with great dynamical, thermal, and mechanical stability. The spin−orbital coupling (SOC) and the out-of-plane asymmetry lead to Rashba spin splitting at the conduction band minimum (CBM), which can be effectively tuned by the small uniaxial strain. The strong band dispersion at the CBM leads to small electron effective mass, consequently enabling a high electron mobility that reaches up to 6816.63 $cm^2\ V^{-1}\ s^{-1}$. Moreover, Janus $Sb_2Se_xTe_{3-x}$ monolayers possess great light absorption capability within the visible and infrared regions of solar light. Our findings highlight promising candidates for high-speed spintronic devices and may motivate more research efforts on carrier transport and SOC effects in Janus group V and VI monolayers.

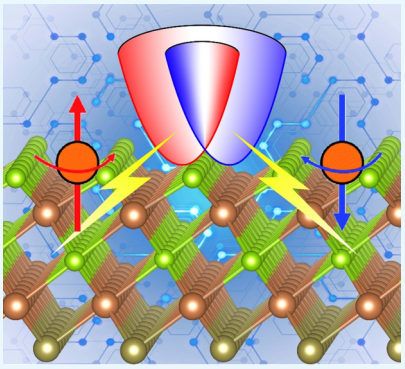

INTRODUCTION

Ever since the discovery of graphene,[1] the 2D world has expanded extensively with numerous novel 2D materials fabricated or predicted.[2−8] An emerging class of 2D materials, Janus materials, has received great research attention recently due to the absence of inversion symmetry along the out-of-plane direction.[9] Various Janus 2D materials have been proposed such as Janus transition metal dichalcogenides (TMDs)[10,11] and Janus group III monochalcogenides M_2XY (M = Ga or In; X/Y = S, Se, or Te),[12,13] displaying versatile properties including magnetism,[14] piezoelectricity,[15] ferroelasticity,[16] valley polarization,[17,18] and Rashba-type spin splitting.[19−22] The Rashba effect describes the momentum-dependent splitting of spin bands that results from the spin−orbital coupling (SOC) in structural inversion asymmetric systems. The Rashba effect offers unique gate tunability over spin precession, which has been experimentally demonstrated in BiTeBr,[23] InSb/CdTe heterostructures,[24] $SrTiO_3$,[25] and $LaAlO_3/SrTiO_3$ interfaces,[26] showing promising applications in novel spintronic devices like spin injectors and spin field-effect transistors.[27,28] The intrinsic inversion asymmetry in Janus 2D materials offers an ideal platform to explore the Rashba SOC down to the 2D regime.[22,29−33] However, the low carrier mobility can limit the practical applications of Janus 2D materials. For example, the electron mobility of Janus TMDs only ranges from ∼70 to ∼245 $cm^2\ V^{-1}\ s^{-1}$,[34] considerably smaller than black phosphorus with a high electron mobility over 2200 $cm^2\ V^{-1}\ s^{-1}$,[35] which hinders their applications in high-speed and fast-response electronic/spintronic devices. Hence, it is of great interest to explore new Janus 2D materials with a strong Rashba effect and high electron mobility.

Previous reports have demonstrated the high electron mobility in centrosymmetric 2D group V and VI layers,[36−38] and most of them contain heavy elements; thus, a strong Rashba effect can be expected if inversion asymmetry is introduced by Janus structural design. In this work, by first-principles calculations, we proposed 2D Janus antimony selenium telluride ($Sb_2Se_xTe_{3-x}$) simultaneously harboring strong Rashba SOC and high electron mobility. Their centrosymmetric bulk counterparts have been experimentally synthesized and display a layered morphology.[39,40] Especially, for Sb_2Se_2Te, there is one experimentally fabricated layered allotrope with intrinsic Janus layers,[41] indicating the high possibility of achieving these Janus monolayers in experiments. The Janus $Sb_2Se_xTe_{3-x}$ monolayers possess robust structures with great dynamical, thermal, and mechanical stability. The lateral asymmetry leads to Rashba spin splitting at the conduction band bottom with large α_R that can be tuned by external strain. They are indirect semiconductors with moderate band gaps (0.90 and 0.85 eV for Sb_2Se_2Te and Sb_2SeTe_2, respectively) and display great light absorption capability. Moreover, the electron mobility of these monolayers surpasses 2000 $cm^2\ V^{-1}\ s^{-1}$ and reaches up to 6816.63 $cm^2\ V^{-1}$

Received: August 27, 2021
Accepted: November 5, 2021
Published: November 18, 2021

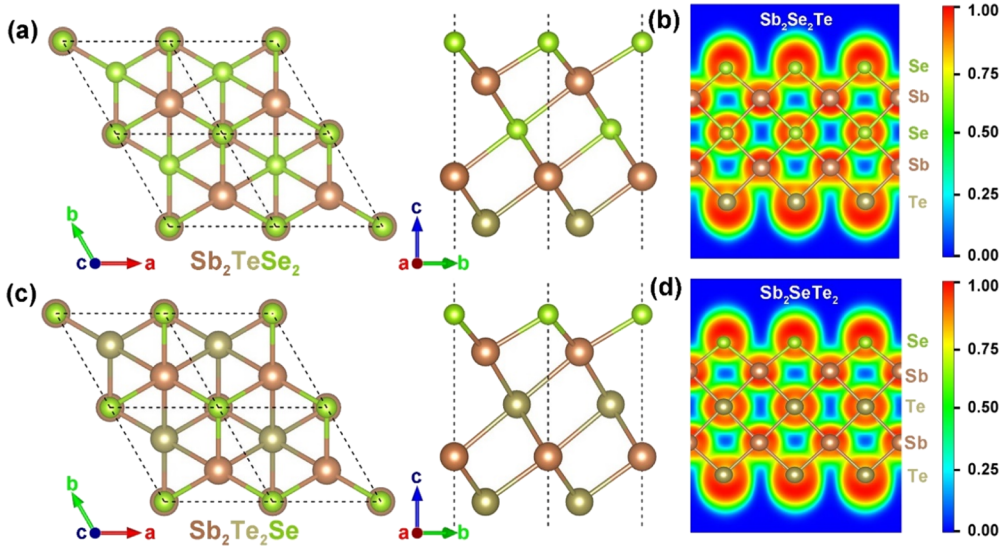

Figure 1. (a, c) Top and side views of Janus Sb_2Se_2Te and Sb_2SeTe_2 monolayers, respectively. (b, d) ELF of Janus Sb_2Se_2Te and Sb_2SeTe_2 monolayers, respectively.

s^{-1}. These novel properties make Janus 2D $Sb_2Se_xTe_{3-x}$ promising candidates for nanoscale spintronics and electronics.

RESULTS AND DISCUSSION

The Janus $Sb_2Se_xTe_{3-x}$ monolayers possess a rhombohedral geometry with a $P3m1$ space group, as shown in Figure 1a,c. Each monolayer consists of five atomic layers following the stacking sequences of Se-Sb-Se-Sb-Te and Se-Sb-Te-Sb-Te for Sb_2Se_2Te and Sb_2SeTe_2, respectively. The lattice parameter and thickness of Sb_2SeTe_2 are larger than those of Sb_2Se_2Te due to the larger atomic radius of Te (see Table 1). The

Table 1. Lattice Parameters, Thicknesses (including the van der Waals Spacing), and Elastic Constants of Janus Sb_2Se_2Te and Sb_2SeTe_2 Monolayers

	lattice parameters (Å)	thickness (Å)	C_{11} (N/m)	C_{12} (N/m)	C_{66} (N/m)
Sb_2Se_2Te	4.12	9.73	70.71	18.01	26.37
Sb_2SeTe_2	4.21	9.83	64.50	18.10	23.17

cohesive energies are calculated to be −3.04 and −2.93 eV/atom for Sb_2Se_2Te and Sb_2SeTe_2, respectively, suggesting the strong bonding characteristics of these monolayers. To further understand the bonding nature of Janus $Sb_2Se_xTe_{3-x}$ monolayers, the electron localization function (ELF) is calculated and shown in Figure 1b,d. The red (1.0), green (0.5), and blue (0.0) regions correspond to fully localized electrons, fully delocalized electrons, and very low charge density, respectively. It is clear that the value of ELF is high around the atomic sites while the value is close to 0.5 in the bonding regions. It is known that in the case of a covalent bond, the lone-pair electrons are localized around the atoms and the electrons constituting the bonds are delocalized. Hence, the Sb−Se and Sb−Te atoms are bonded by forming covalent bonds, which is similar to the bonding nature of Bi_2Te_2Se and Bi_2Se_2Te.[42]

The phonon spectra of $Sb_2Se_xTe_{3-x}$ are shown in Figure 2a,b, respectively. Clearly, there is no negative frequency in the spectra, which demonstrates the dynamical stability of these monolayers. Their thermal stability is also confirmed by the

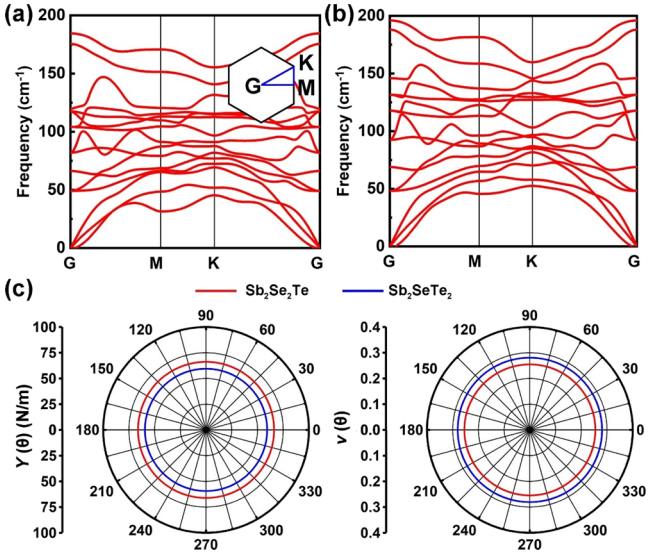

Figure 2. (a, b) Phonon spectra of Janus Sb_2Se_2Te and Sb_2SeTe_2 monolayers, respectively. The inset represents the Brillouin zone marking the high symmetry k-points. (c) Young's modulus and Poisson's ratio of Janus $Sb_2Se_xTe_{3-x}$ monolayers as functions of the in-plane angle θ.

AIMD (ab initio molecular dynamics) simulations of 5 ps performed at 300 K (as shown in Figure S1), where the structures and total energy only fluctuate slightly during the simulations. Moreover, the calculated elastic constants of Janus $Sb_2Se_xTe_{3-x}$ (Table 1) fulfill the Born mechanical stability criteria and suggest their mechanical stability.[43] The in-plane Young's modulus (Y) and Poisson's ratio (ν) as a function of in-plane θ (the angle between applied uniaxial strain and lattice a) can be determined by the following two equations, respectively:[44,45]

$$Y(\theta) = \frac{C_{11}C_{22} - C_{12}^2}{C_{11}\sin^4\theta + A\sin^2\theta\cos^2\theta + C_{22}\cos^4\theta} \quad (1)$$

https://doi.org/10.1021/acsomega.1c04680
ACS Omega 2021, 6, 31919−31925

$$\nu(\theta) = \frac{C_{12}\sin^4\theta - B\sin^2\theta\cos^2\theta + C_{12}\cos^4\theta}{C_{11}\sin^4\theta + A\sin^2\theta\cos^2\theta + C_{22}\cos^4\theta} \quad (2)$$

where $A = (C_{11}C_{22} - C_{12}^2)/C_{66} - 2C_{12}$ and $B = C_{11} + C_{22} - (C_{11}C_{22} - C_{12}^2)/C_{66}$. The calculated direction-dependent Y and ν are shown in Figure 2c. The Y (ν) values of Janus Sb_2Se_2Te and Sb_2SeTe_2 monolayers are calculated to be 66.15 N/m (0.25) and 59.38 N/m (0.28), respectively, along all directions, suggesting that these Janus monolayers are mechanically isotropic. Noticeably, the Y values of Janus $Sb_2Se_xTe_{3-x}$ monolayers are far smaller than those of graphene (335 N/m), BN (267 N/m),[46] and MoS_2 (180 ± 60 N/m),[47] offering the opportunity to tune their electronic structures by applying strain.

Having confirmed the stability of Janus $Sb_2Se_xTe_{3-x}$ monolayers, we then focus on their electronic structures. Figure 3 shows the band structures calculated by the HSE06

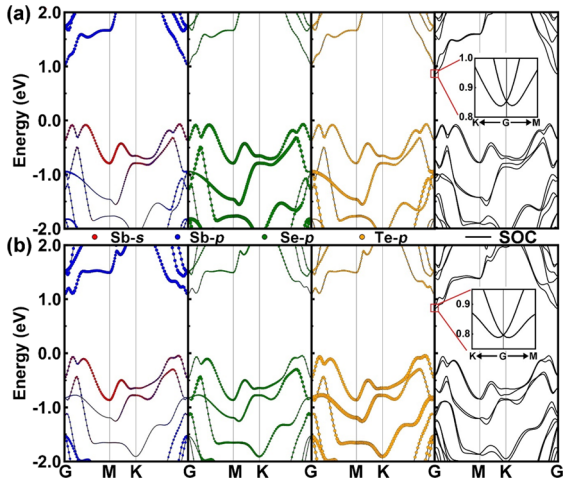

Figure 3. (a, b) Orbital resolved band structures calculated without SOC and band structures with SOC by the HSE06 functional for Sb_2Se_2Te and Sb_2SeTe_2, respectively. The insets are the zoomed-in view of the conduction band minimum around the gamma point.

functional with/without the inclusion of SOC. Janus 2D Sb_2Se_2Te and Sb_2SeTe_2 monolayers are indirect semiconductors with band gaps of 1.10 and 1.14 eV, respectively. They display similar band compositions near the Fermi level, with the valence band top composed of Sb-s, Se-p, and Te-p orbitals while the conduction band bottom being mainly contributed by the Sb-p orbitals. The CBM is located at the gamma point, while the valence band maximum (VBM) is found along the K-G path. The inclusion of SOC leads to spin splitting of the electronic bands, and the band gaps are reduced to 0.90 and 0.85 eV for 2D Sb_2Se_2Te and Sb_2SeTe_2, respectively. We also calculated the band structures with SOC using the GW method for comparison (shown in Figure S2), which shows perfect consistency with those calculated by the HSE06 functional. Remarkably, a Rashba-type spin splitting of the conduction band at the gamma point is observed, as we will detailedly discuss below.

To confirm the Rashba spin splitting at the CBM, the 2D constant energy contour of the spin texture is calculated in a k_x–k_y plane centered at the gamma point, as shown in Figure 4a–c and Figure S3. Clearly, the spin-up (red) and spin-down (blue) conduction bands split, resulting in concentric spin-texture circles in the 2D k-mesh. It is found that the energy

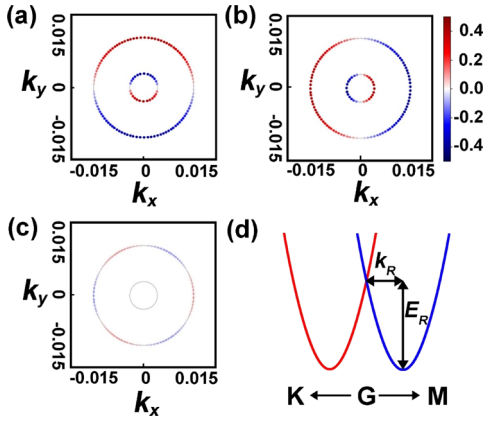

Figure 4. (a–c) Projection of spin components S_X, S_Y, and S_Z for Sb_2Se_2Te at a constant energy contour of 0.05 eV higher than the CBM calculated by the PBE functional, respectively. (d) Schematic of the energy dispersion of Rashba spin splitting at the CBM, and the Rashba energy E_R and Rashba momentum k_R.

bands are mainly composed of the in-plane S_X and S_Y spin components, with a negligible out-of-plane S_Z component. The in-plane spin orientation is found perpendicular to the direction of the k vectors, which is a typical signature of Rashba-type spin splitting.[27] The Rashba parameter α_R, which evaluates the strength of the Rashba effect, can then be obtained from the formula $\alpha_R = 2E_R/k_R$ based on a linear Rashba model, where E_R and k_R represent the Rashba energy and Rashba momentum, respectively, as indicated in Figure 4d. The α_R along the arm-chair ($\alpha_R^{\mathrm{arm-chair}}$) and zig-zag ($\alpha_R^{\mathrm{zig-zag}}$) directions are calculated separately. The calculated values of $\alpha_R^{\mathrm{arm-chair}}$ are 1.53 and 1.00 eV Å while the calculated values of $\alpha_R^{\mathrm{zig-zag}}$ are 1.52 and 1.12 eV Å for Janus Sb_2Se_2Te and Sb_2SeTe_2 monolayers, respectively. Clearly, the α_R is nearly isotropic for Sb_2Se_2Te while it is anisotropic for Sb_2SeTe_2. The α_R values of Janus Sb_2Se_2Te and Sb_2SeTe_2 monolayers are much larger than those of Janus transition metal dichalcogenides (0.08–0.51 eV Å),[22] Janus TiBrI (0.15 eV Å),[30] and Janus Te_2Se (0.39 eV Å)[31] and comparable to those of Janus TiS_2Se (1.08 eV Å),[29] Janus SbTeI (1.39 eV Å),[33] and Janus PBi (1.56 eV Å),[32] suggesting the promising applications of Janus $Sb_2Se_xTe_{3-x}$ monolayers in spintronic devices like spin-polarized field-effect transistors.[27,28]

We then explored the effect of uniaxial strain along the arm-chair ($\varepsilon_{\mathrm{arm-chair}}$) and zig-zag ($\varepsilon_{\mathrm{zig-zag}}$) directions on the Rashba SOC in our systems. The negative values indicate compressive strain, while the positive values represent tensile strain. As shown in Figure 5, we can find that there is a general trend where an increase in uniaxial strain would lead to the decrease in E_R and k_R along the strain direction and the increase in E_R and k_R along the vertical direction. Generally, a larger E_R is desirable for stabilizing electron spin while a larger k_R will benefit the phase offset for different spin channels, which are favorable for spin transport. Through applying uniaxial strain, the stability of electron spin and phase offset can then be enhanced (suppressed) along the strain direction but suppressed (enhanced) along the vertical direction, which may favor the anisotropic spin transport.

When uniaxial strain is applied, the α_R for both Janus Sb_2Se_2Te and Sb_2SeTe_2 monolayers becomes anisotropic, as shown in Figure 6. The strength of α_R can be tuned more significantly if they lie in the same direction with the external

https://doi.org/10.1021/acsomega.1c04680
ACS Omega 2021, 6, 31919–31925

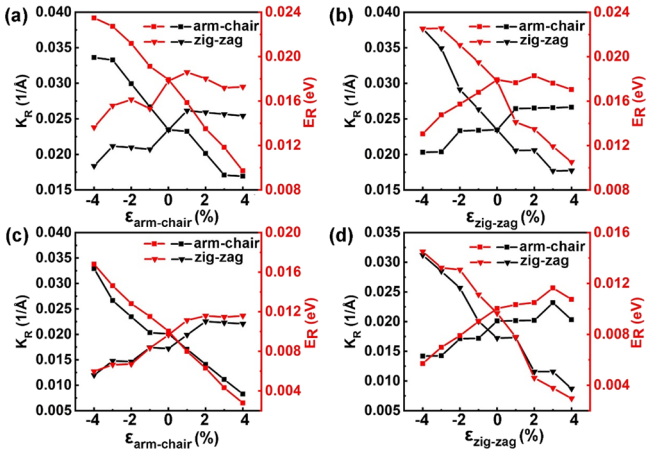

Figure 5. (a, b) E_R and k_R of Janus Sb_2Se_2Te monolayers under different uniaxial strains applied along the arm-chair and zig-zag directions, respectively. (c, d) E_R and k_R of Janus Sb_2SeTe_2 monolayers under different uniaxial strains applied along the arm-chair and zig-zag directions, respectively.

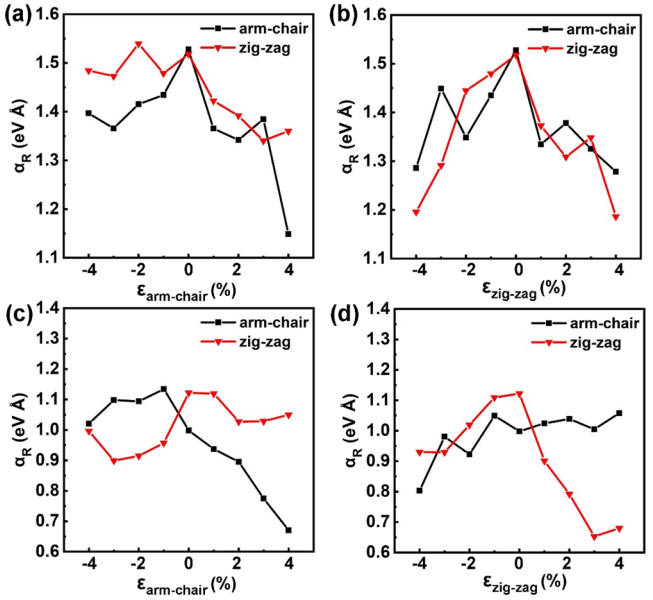

Figure 6. (a, b) α_R of Janus Sb_2Se_2Te monolayers under different uniaxial strains applied along the arm-chair and zig-zag directions, respectively. (c, d) α_R of Janus Sb_2SeTe_2 monolayers under different uniaxial strains applied along the arm-chair and zig-zag directions, respectively.

uniaxial strain. For Janus Sb_2Se_2Te, the $\alpha_R^{arm-chair}$ reaches the maximum at the equilibrium state (1.53 eV Å) and the minimum at $\varepsilon_{arm-chair}$ = 4% (1.15 eV Å), while the $\alpha_R^{zig-zag}$ reaches the maximum at $\varepsilon_{arm-chair}$ = −2% (1.54 eV Å) and the minimum at $\varepsilon_{zig-zag}$ = −4% (1.20 eV Å). For Janus Sb_2SeTe_2, the $\alpha_R^{arm-chair}$ reaches the maximum at the $\varepsilon_{arm-chair}$ = −1% (1.13 eV Å) and the minimum at $\varepsilon_{arm-chair}$ = 4% (0.67 eV Å), while the $\alpha_R^{zig-zag}$ reaches the maximum at the equilibrium state (1.12 eV Å) and the minimum at $\varepsilon_{zig-zag}$ = 3% (0.65 eV Å). The strong Rashba SOC tunable by external strain makes Janus $Sb_2Se_xTe_{3-x}$ monolayers promising candidates for nanoscale spintronic devices.

The conduction band near the CBM displays rather strong disperse along the G-M and K-G paths, which correspond, respectively, to the arm-chair and zig-zag directions in the real space, indicating the small effective mass along with these directions. Fitting these bands (with SOC) using a free electron model, the effective carrier mass of 2D Sb_2Se_2Te (Sb_2SeTe_2) is calculated to be 0.14 (0.15) m_0 along the arm-chair direction and 0.15 (0.15) m_0 along the zig-zag direction. These values are comparable to other high-mobility semiconductors such as black phosphorene (0.14−0.18 m_0)[35] and AlGaAs (0.1 m_0),[48] inspiring us to explore the electron mobility of these monolayers.

The electron mobility (μ) is calculated based on the phonon-limited scattering model, in the formula, as shown below, which incorporates the anisotropy of the deformation potential:[49]

$$\mu_x = \frac{e\hbar^3\left(\frac{5C_{2Dx}+3C_{2Dy}}{8}\right)}{k_BT(m_x)^{3/2}(m_y)^{1/2}\left(\frac{9(E_x)^2+7E_xE_y+4(E_y)^2}{20}\right)} \quad (3)$$

where e is the electron charge, $\hbar$ is the reduced Plank constant, k_B is the Boltzmann constant, and T is the temperature. C_{2D} and m are the elastic constant and effective mass of the electron along the transport direction. E is the deformation potential of the CBM in the transport direction, calculated by $E = \Delta V/(\Delta l/l_0)$, where l_0 is the lattice constant along the transport direction and ΔV is the change of CBM positions upon deformation Δl. The subscripts x and y mark the directions (arm-chair/zig-zag directions). The three parameters effective mass, elastic constants, and deformation potential are the most relevant factors in determining the mobility, as we can see in eq 3. We show these parameters together with the electron mobility in Table 2. The calculated electron mobilities

Table 2. In-Plane Stiffness (C), Effective Mass of Charge Carriers (m), Deformation Potential (E) (as Shown in Figure S4), and Electron Mobility (μ) of Sb_2Se_2Te and Sb_2SeTe_2 Monolayers at 300 K

	direction	C (N/m)	E (eV)	m (m_0)	μ (cm^2V^{-1} s^{-1})
Sb_2Se_2Te	arm-chair	70.71	5.85	0.14	2310.98
	zig-zag	70.71	5.36	0.15	2253.25
Sb_2SeTe_2	arm-chair	64.50	3.89	0.15	5414.73
	zig-zag	64.50	2.42	0.15	6816.63

along the arm-chair (zig-zag) direction are 2310.98 (2253.25) and 5414.73 (6816.63) cm^2 V^{-1} s^{-1} for Janus Sb_2Se_2Te and Sb_2SeTe_2 monolayers, respectively. These values are larger than or comparable to many reported Janus 2D materials including Janus MXY (M = Mo or W; X/Y = S, Se, or Te; and X ≠ Y) (70−245 cm^2 V^{-1} s^{-1}),[34] Janus MXY (M = Ti, Zr, or Hf; X = S or Se; Y = O or S; X ≠ Y) (1−430 cm^2 V^{-1} s^{-1}),[50] Janus PtSSe (1546.52 cm^2 V^{-1} s^{-1}),[51] Janus PtXO (X = S or Se) (2164.95 cm^2 V^{-1} s^{-1}),[52] and Janus In_2SO (3428 cm^2 V^{-1} s^{-1}),[53] offering great potential for high-speed electronic devices.[54]

Janus $Sb_2Se_xTe_{3-x}$ with moderate band gaps are expected to exhibit excellent optical properties. Figure 7 shows the optical absorption spectra of Janus $Sb_2Se_xTe_{3-x}$ calculated by the GW-BSE method with the inclusion of SOC and excitonic effects. Both monolayers possess great light absorbance in the whole visible light range. The light absorption onsets are determined to be around 1350 and 1670 nm for Sb_2Se_2Te and Sb_2SeTe_2, respectively, which lie within the infrared region of solar light. The strong absorption at the long-wavelength range may be

https://doi.org/10.1021/acsomega.1c04680
ACS Omega 2021, 6, 31919−31925

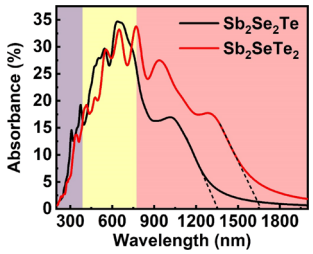

Figure 7. Light absorption spectra of Janus Sb_2Se_2Te and Sb_2SeTe_2 monolayers. The light absorption onsets are estimated by a linear extrapolation method as indicated by the dashed lines. The purple, yellow, and pink areas mark the ultraviolet, visible, and infrared regions of solar light, respectively.

attributed to the transition from the occupied s orbital of Sb and p orbital of Se/Te to the unoccupied p orbital of Sb based on the electronic structures in Figure 3. Because the infrared region accounts for more than half of the solar energy, these two monolayers show promising applications in photovoltaic devices such as high-efficiency light-absorbers.

CONCLUSIONS

In summary, we have investigated the electronic structure and electron mobility of Janus $Sb_2Se_xTe_{3-x}$ monolayers by DFT calculations. They exhibit great dynamical, thermal, and mechanical stability. It is found that Janus 2D Sb_2Se_2Te and Sb_2SeTe_2 are indirect semiconductors with band gaps of 0.90 and 0.85 eV, respectively. The inversion asymmetry of the Janus structures leads to Rashba spin splitting at the CBM, with large α_R values reaching up to 1.53 and 1.12 eV Å for Sb_2Se_2Te and Sb_2SeTe_2, respectively. Moreover, the Rashba SOC of Janus $Sb_2Se_xTe_{3-x}$ can be sufficiently tuned with a small uniaxial strain. The carrier mobility of these Janus monolayers is high (>2000 $cm^2\ V^{-1}\ s^{-1}$) due to the small effective mass at the CBM. In addition, both monolayers possess extraordinary light absorption ability. Our work reveals the large Rashba spin splitting and high electron mobility in Janus 2D Sb_2Se_2Te and Sb_2SeTe_2, which shows promising applications in ultrafast nanoscale spintronics and may stimulate more research efforts on the novel electronic and transport properties of Janus group V and VI compounds.

COMPUTATIONAL METHODS

The DFT calculations were performed by using the Vienna Ab-initio Simulation Package (VASP).[55−57] The exchange−correlation interaction was described by the generalized gradient approximation (GGA) of the Perdew−Burke−Ernzerhof (PBE)-type functional.[58,59] The projector augmented wave (PAW) method[60] was applied to treat the electron−core interactions. The van der Waals (vdW) dispersion was included by the Grimme method (DFT-D3).[61] The cutoff energy for plane waves was set to 400 eV, and a 9 × 9 × 1 *k*-point mesh was applied to sample the first Brillouin zone. A vacuum space around 18 Å was used to exclude the influence of neighboring images induced by the periodic boundary conditions. The structures were fully relaxed until the residual forces and the energy were converged to 0.005 eV/Å and 1×10^{-6} eV, respectively. The electronic structure was calculated by the Heyd−Scuseria−Ernzerhof (HSE06) hybrid functional with the SOC effect taken into consideration.[62] The optical absorption spectrum was obtained by using single-shot GW (G0W0) with the Bethe−Salpeter equation (BSE) approach, which includes many-body effects.[63,64] The phonon spectrum was calculated by the density functional perturbation theory method[65] as implemented in the Quantum ESPRESSO code.[66,67] The AIMD simulation was carried out for 5 ps with a time step of 1.0 fs in the NVT ensemble, and the Langevin thermostat[68,69] was used to control the temperature. The AIMD simulation was performed using a 5 × 5 × 1 supercell, and only the gamma point was included in the *k*-point mesh.

ASSOCIATED CONTENT

Supporting Information

The Supporting Information is available free of charge at https://pubs.acs.org/doi/10.1021/acsomega.1c04680.

AIMD results; band structures calculated by the GW method; projection of spin components at a constant energy contour; linear fitting of deformation potential; and light absorbance calculated with different vacuum thicknesses (PDF)

AUTHOR INFORMATION

Corresponding Author

Aijun Du − *School of Chemistry and Physics and Centre for Materials Science, Queensland University of Technology, Brisbane, QLD 4000, Australia;* orcid.org/0000-0002-3369-3283; Email: aijun.du@qut.edu.au

Authors

Lei Zhang − *School of Chemistry and Physics and Centre for Materials Science, Queensland University of Technology, Brisbane, QLD 4000, Australia*

Yuantong Gu − *School of Mechanical, Medical and Process Engineering, Queensland University of Technology, Brisbane, QLD 4000, Australia*

Complete contact information is available at: https://pubs.acs.org/10.1021/acsomega.1c04680

Notes

The authors declare no competing financial interest.

ACKNOWLEDGMENTS

We acknowledge generous grants of high-performance computing resources provided by the NCI National Facility and the Pawsey Supercomputing Centre through the National Computational Merit Allocation Scheme supported by the Australian Government and the Government of Western Australia. A.D. also greatly appreciates the financial support of the Australian Research Council under Discovery Project (DP170103598, DP210100721, and DP210100331).

REFERENCES

(1) Novoselov, K. S.; Geim, A. K.; Morozov, S. V.; Jiang, D.; Zhang, Y.; Dubonos, S. V.; Grigorieva, I. V.; Firsov, A. A. Electric Field Effect in Atomically Thin Carbon Films. *Science* **2004**, *306*, 666−669.

(2) Mak, K. F.; Lee, C.; Hone, J.; Shan, J.; Heinz, T. F. Atomically Thin MoS_2: A New Direct-Gap Semiconductor. *Phys. Rev. Lett.* **2010**, *105*, 136805.

(3) Gong, C.; Li, L.; Li, Z.; Ji, H.; Stern, A.; Xia, Y.; Cao, T.; Bao, W.; Wang, C.; Wang, Y.; Qiu, Z. Q.; Cava, R. J.; Louie, S. G.; Xia, J.; Zhang, X. Discovery of Intrinsic Ferromagnetism in Two-Dimensional Van Der Waals Crystals. *Nature* **2017**, *546*, 265.

(4) Huang, B.; Clark, G.; Navarro-Moratalla, E.; Klein, D. R.; Cheng, R.; Seyler, K. L.; Zhong, D.; Schmidgall, E.; McGuire, M. A.; Cobden,

D. H.; Yao, W.; Xiao, D.; Jarillo-Herrero, P.; Xu, X. Layer-Dependent Ferromagnetism in a Van Der Waals Crystal Down to the Monolayer Limit. *Nature* **2017**, *546*, 270.
(5) Wang, Q. H.; Kalantar-Zadeh, K.; Kis, A.; Coleman, J. N.; Strano, M. S. Electronics and Optoelectronics of Two-Dimensional Transition Metal Dichalcogenides. *Nat. Nanotechnol.* **2012**, *7*, 699−712.
(6) Li, L.; Yu, Y.; Ye, G. J.; Ge, Q.; Ou, X.; Wu, H.; Feng, D.; Chen, X. H.; Zhang, Y. Black Phosphorus Field-Effect Transistors. *Nat. Nanotechnol.* **2014**, *9*, 372−377.
(7) Frey, N. C.; Kumar, H.; Anasori, B.; Gogotsi, Y.; Shenoy, V. B. Tuning Noncollinear Spin Structure and Anisotropy in Ferromagnetic Nitride MXenes. *ACS Nano* **2018**, *12*, 6319−6325.
(8) Hong, Y. L.; Liu, Z.; Wang, L.; Zhou, T.; Ma, W.; Xu, C.; Feng, S.; Chen, L.; Chen, M. L.; Sun, D. M.; Chen, X. Q.; Cheng, H. M.; Ren, W. Chemical Vapor Deposition of Layered Two-Dimensional $MoSi_2N_4$ Materials. *Science* **2020**, *369*, 670−674.
(9) Zhang, L.; Yang, Z.; Gong, T.; Pan, R.; Wang, H.; Guo, Z.; Zhang, H.; Fu, X. Recent Advances in Emerging Janus Two-Dimensional Materials: From Fundamental Physics to Device Applications. *J. Mater. Chem. A* **2020**, *8*, 8813−8830.
(10) Lu, A.-Y.; Zhu, H.; Xiao, J.; Chuu, C.-P.; Han, Y.; Chiu, M.-H.; Cheng, C.-C.; Yang, C.-W.; Wei, K.-H.; Yang, Y.; Wang, Y.; Sokaras, D.; Nordlund, D.; Yang, P.; Muller, D. A.; Chou, M.-Y.; Zhang, X.; Li, L.-J. Janus Monolayers of Transition Metal Dichalcogenides. *Nat. Nanotechnol.* **2017**, *12*, 744−749.
(11) Zhang, J.; Jia, S.; Kholmanov, I.; Dong, L.; Er, D.; Chen, W.; Guo, H.; Jin, Z.; Shenoy, V. B.; Shi, L.; Lou, J. Janus Monolayer Transition-Metal Dichalcogenides. *ACS Nano* **2017**, *11*, 8192−8198.
(12) Kandemir, A.; Sahin, H. Janus Single Layers of In_2SSe: A First-Principles Study. *Phys. Rev. B* **2018**, *97*, 155410.
(13) Huang, A.; Shi, W.; Wang, Z. Optical Properties and Photocatalytic Applications of Two-Dimensional Janus Group-III Monochalcogenides. *J. Phys. Chem. C* **2019**, *123*, 11388−11396.
(14) Frey, N. C.; Bandyopadhyay, A.; Kumar, H.; Anasori, B.; Gogotsi, Y.; Shenoy, V. B. Surface-Engineered MXenes: Electric Field Control of Magnetism and Enhanced Magnetic Anisotropy. *ACS Nano* **2019**, *13*, 2831−2839.
(15) Dong, L.; Lou, J.; Shenoy, V. B. Large In-Plane and Vertical Piezoelectricity in Janus Transition Metal Dichalchogenides. *ACS Nano* **2017**, *11*, 8242−8248.
(16) Zhang, C.; Nie, Y.; Sanvito, S.; Du, A. First-Principles Prediction of a Room-Temperature Ferromagnetic Janus VSSe Monolayer with Piezoelectricity, Ferroelasticity, and Large Valley Polarization. *Nano Lett.* **2019**, *19*, 1366−1370.
(17) Qi, S.; Jiang, J.; Wang, X.; Mi, W. Valley Polarization, Magnetic Anisotropy and Dzyaloshinskii-Moriya Interaction of Two-Dimensional Graphene/Janus 2H-VSeX (X = S, Te) Heterostructures. *Carbon* **2021**, *174*, 540−555.
(18) Peng, R.; Ma, Y.; Zhang, S.; Huang, B.; Dai, Y. Valley Polarization in Janus Single-Layer MoSSe Via Magnetic Doping. *J. Phys. Chem. Lett.* **2018**, *9*, 3612−3617.
(19) Liu, M.-Y.; Gong, L.; He, Y.; Cao, C. Tuning Rashba Effect, Band Inversion, and Spin-Charge Conversion of Janus XSn_2Y Monolayers Via an External Field. *Phys. Rev. B* **2021**, *103*, No. 075421.
(20) Babaee Touski, S.; Ghobadi, N. Structural, Electrical, and Rashba Properties of Monolayer Janus Si_2XY (X,Y=P, as, Sb, and Bi). *Phys. Rev. B* **2021**, *103*, 165404.
(21) Yao, Q.-F.; Cai, J.; Tong, W.-Y.; Gong, S.-J.; Wang, J.-Q.; Wan, X.; Duan, C.-G.; Chu, J. H. Manipulation of the Large Rashba Spin Splitting in Polar Two-Dimensional Transition-Metal Dichalcogenides. *Phys. Rev. B* **2017**, *95*, 165401.
(22) Hu, T.; Jia, F.; Zhao, G.; Wu, J.; Stroppa, A.; Ren, W. Intrinsic and Anisotropic Rashba Spin Splitting in Janus Transition-Metal Dichalcogenide Monolayers. *Phys. Rev. B* **2018**, *97*, 235404.
(23) Kovács-Krausz, Z.; Hoque, A. M.; Makk, P.; Szentpéteri, B.; Kocsis, M.; Fülöp, B.; Yakushev, M. V.; Kuznetsova, T. V.; Tereshchenko, O. E.; Kokh, K. A.; Lukács, I. E.; Taniguchi, T.; Watanabe, K.; Dash, S. P.; Csonka, S. Electrically Controlled Spin Injection from Giant Rashba Spin−Orbit Conductor Bitebr. *Nano Lett.* **2020**, *20*, 4782−4791.
(24) Zhang, Y.; Xue, F.; Tang, C.; Li, J.; Liao, L.; Li, L.; Liu, X.; Yang, Y.; Song, C.; Kou, X. Highly Efficient Electric-Field Control of Giant Rashba Spin−Orbit Coupling in Lattice-Matched InSb/CdTe Heterostructures. *ACS Nano* **2020**, *14*, 17396−17404.
(25) Noël, P.; Trier, F.; Vicente Arche, L. M.; Bréhin, J.; Vaz, D. C.; Garcia, V.; Fusil, S.; Barthélémy, A.; Vila, L.; Bibes, M.; Attané, J.-P. Non-Volatile Electric Control of Spin−Charge Conversion in a $SrTiO_3$ Rashba System. *Nature* **2020**, *580*, 483−486.
(26) Choe, D.; Jin, M.-J.; Kim, S.-I.; Choi, H.-J.; Jo, J.; Oh, I.; Park, J.; Jin, H.; Koo, H. C.; Min, B.-C.; Hong, S.; Lee, H.-W.; Baek, S.-H.; Yoo, J.-W. Gate-Tunable Giant Nonreciprocal Charge Transport in Noncentrosymmetric Oxide Interfaces. *Nat. Commun.* **2019**, *10*, 4510.
(27) Manchon, A.; Koo, H. C.; Nitta, J.; Frolov, S. M.; Duine, R. A. New Perspectives for Rashba Spin−Orbit Coupling. *Nat. Mater.* **2015**, *14*, 871−882.
(28) Koo, H. C.; Kim, S. B.; Kim, H.; Park, T.-E.; Choi, J. W.; Kim, K.-W.; Go, G.; Oh, J. H.; Lee, D.-K.; Park, E.-S.; Hong, I.-S.; Lee, K.-J. Rashba Effect in Functional Spintronic Devices. *Adv. Mater.* **2020**, *32*, 2002117.
(29) Ahammed, R.; Jena, N.; Rawat, A.; Mohanta, M. K.; Dimple; De Sarkar, A. Ultrahigh out-of-Plane Piezoelectricity Meets Giant Rashba Effect in 2D Janus Monolayers and Bilayers of Group IV Transition-Metal Trichalcogenides. *J. Phys. Chem. C* **2020**, *124*, 21250−21260.
(30) Wang, Y.; Wei, W.; Wang, H.; Mao, N.; Li, F.; Huang, B.; Dai, Y. Janus TiXY Monolayers with Tunable Berry Curvature. *J. Phys. Chem. Lett.* **2019**, *10*, 7426−7432.
(31) Chen, Y.; Liu, J.; Yu, J.; Guo, Y.; Sun, Q. Symmetry-Breaking Induced Large Piezoelectricity in Janus Tellurene Materials. *Phys. Chem. Chem. Phys.* **2019**, *21*, 1207−1216.
(32) Zhu, L.; Zhang, T.; Chen, G.; Chen, H. Huge Rashba-Type Spin−Orbit Coupling in Binary Hexagonal PX Nanosheets (X = As, Sb, and Bi). *Phys. Chem. Chem. Phys.* **2018**, *20*, 30133−30139.
(33) Zhuang, H. L.; Cooper, V. R.; Xu, H.; Ganesh, P.; Hennig, R. G.; Kent, P. R. C. Rashba Effect in Single-Layer Antimony Telluroiodide SbTeI. *Phys. Rev. B* **2015**, *92*, 115302.
(34) Wang, J.; Shu, H.; Zhao, T.; Liang, P.; Wang, N.; Cao, D.; Chen, X. Intriguing Electronic and Optical Properties of Two-Dimensional Janus Transition Metal Dichalcogenides. *Phys. Chem. Chem. Phys.* **2018**, *20*, 18571−18578.
(35) Qiao, J.; Kong, X.; Hu, Z.-X.; Yang, F.; Ji, W. High-Mobility Transport Anisotropy and Linear Dichroism in Few-Layer Black Phosphorus. *Nat. Commun.* **2014**, *5*, 4475.
(36) Wu, J.; Yuan, H.; Meng, M.; Chen, C.; Sun, Y.; Chen, Z.; Dang, W.; Tan, C.; Liu, Y.; Yin, J.; Zhou, Y.; Huang, S.; Xu, H. Q.; Cui, Y.; Hwang, H. Y.; Liu, Z.; Chen, Y.; Yan, B.; Peng, H. High Electron Mobility and Quantum Oscillations in Non-Encapsulated Ultrathin Semiconducting Bi_2O_2Se. *Nat. Nanotechnol.* **2017**, *12*, 530−534.
(37) Wang, B.; Niu, X.; Ouyang, Y.; Zhou, Q.; Wang, J. Ultrathin Semiconducting Bi_2Te_2S and Bi_2Te_2Se with High Electron Mobilities. *J. Phys. Chem. Lett.* **2018**, *9*, 487−490.
(38) Zhang, X.; Wang, B.; Niu, X.; Li, Y.; Chen, Y.; Wang, J. Bi_2OS_2: A Direct-Gap Two-Dimensional Semiconductor with High Carrier Mobility and Surface Electron States. *Mater. Horiz.* **2018**, *5*, 1058−1064.
(39) Gosain, D. P.; Shimizu, T.; Ohmura, M.; Suzuki, M.; Bando, T.; Okano, S. Some Properties of $Sb_2Te_{3-x}Se_x$ for Nonvolatile Memory Based on Phase Transition. *J. Mater. Sci.* **1991**, *26*, 3271−3274.
(40) Anderson, T. L.; Krause, H. B. Refinement of the Sb_2Te_3 and Sb_2Te_2Se Structures and Their Relationship to Nonstoichiometric $Sb_2Te_{3-y}Se_y$ Compounds. *Acta Crystallogr., Sect. B: Struct. Crystallogr. Cryst. Chem.* **1974**, *30*, 1307−1310.
(41) Andriamihaja, A.; Ibanez, A.; Jumas, J. C.; Olivier-Fourcade, J.; Philippot, E. Evolution Structurale De La Solution Solide $Sb_2Te_{3-x}Se_x$ ($0 \leq x \leq 2$) Dans Le Système Sb_2Te_3-Sb_2Se_3. *Rev. Chim. Miner.* **1985**, *22*, 357−368.

https://doi.org/10.1021/acsomega.1c04680
ACS Omega 2021, 6, 31919−31925

(42) Ruan, Y.; Huang, L.; Yang, Y.; Xu, G.; Zhong, K.; Huang, Z.; Zhang, J.-M. Robustness of the Electronic Structure and Charge Transfer in Topological Insulator Bi_2Te_2Se and Bi_2Se_2Te Thin Films under an External Electric Field. *Phys. Chem. Chem. Phys.* **2020**, *22*, 3867−3874.
(43) Mouhat, F.; Coudert, F.-X. Necessary and Sufficient Elastic Stability Conditions in Various Crystal Systems. *Phys. Rev. B* **2014**, *90*, 224104.
(44) Peng, R.; Ma, Y.; He, Z.; Huang, B.; Kou, L.; Dai, Y. Single-Layer Ag_2S: A Two-Dimensional Bidirectional Auxetic Semiconductor. *Nano Lett.* **2019**, *19*, 1227−1233.
(45) Zhang, L.; Tang, C.; Zhang, C.; Gu, Y.; Du, A. First-Principles Prediction of Ferroelasticity Tuned Anisotropic Auxeticity and Carrier Mobility in Two-Dimensional AgO. *J. Mater. Chem. C* **2021**, *9*, 3155−3160.
(46) Şahin, H.; Cahangirov, S.; Topsakal, M.; Bekaroglu, E.; Akturk, E.; Senger, R. T.; Ciraci, S. Monolayer Honeycomb Structures of Group-IV Elements and III-V Binary Compounds: First-Principles Calculations. *Phys. Rev. B* **2009**, *80*, 155453.
(47) Bertolazzi, S.; Brivio, J.; Kis, A. Stretching and Breaking of Ultrathin MoS2. *ACS Nano* **2011**, *5*, 9703−9709.
(48) Walukiewicz, W.; Ruda, H. E.; Lagowski, J.; Gatos, H. C. Electron Mobility in Modulation-Doped Heterostructures. *Phys. Rev. B* **1984**, *30*, 4571−4582.
(49) Lang, H.; Zhang, S.; Liu, Z. Mobility Anisotropy of Two-Dimensional Semiconductors. *Phys. Rev. B* **2016**, *94*, 235306.
(50) Chen, W.; Hou, X.; Shi, X.; Pan, H. Two-Dimensional Janus Transition Metal Oxides and Chalcogenides: Multifunctional Properties for Photocatalysts, Electronics, and Energy Conversion. *ACS Appl. Mater. Interfaces* **2018**, *10*, 35289−35295.
(51) Peng, R.; Ma, Y.; Huang, B.; Dai, Y. Two-Dimensional Janus PtSSe for Photocatalytic Water Splitting under the Visible or Infrared Light. *J. Mater. Chem. A* **2019**, *7*, 603−610.
(52) Shen, H.; Zhang, Y.; Wang, G.; Ji, W.; Xue, X.; Zhang, W. Janus PtXO (X = S, Se) Monolayers: The Visible Light Driven Water Splitting Photocatalysts with High Carrier Mobilities. *Phys. Chem. Chem. Phys.* **2021**, *23*, 21825−21832.
(53) Vu, T. V.; Nguyen, C. V.; Phuc, H. V.; Lavrentyev, A. A.; Khyzhun, O. Y.; Hieu, N. V.; Obeid, M. M.; Rai, D. P.; Tong, H. D.; Hieu, N. N. Theoretical Prediction of Electronic, Transport, Optical, and Thermoelectric Properties of Janus Monolayers In_2XO (X = S, Se, Te). *Phys. Rev. B* **2021**, *103*, No. 085422.
(54) Rajabali, M.; Esfandiari, M.; Rajabali, S.; Vakili-Tabatabaei, M.; Mohajerzadeh, S.; Mohajerzadeh, S. High-Performance Phosphorene-Based Transistors Using a Novel Exfoliation-Free Direct Crystallization on Silicon Substrates. *Adv. Mater. Interfaces* **2020**, *7*, 2000774.
(55) Kresse, G.; Furthmüller, J. Efficiency of Ab-Initio Total Energy Calculations for Metals and Semiconductors Using a Plane-Wave Basis Set. *Comput. Mater. Sci.* **1996**, *6*, 15−50.
(56) Kresse, G.; Furthmüller, J. Efficient iterative schemes for ab initio total-energy calculations using a plane-wave basis set. *Phys. Rev. B* **1996**, *54*, 11169−11186.
(57) Kresse, G.; Hafner, J. Ab Initio Molecular-Dynamics Simulation of the Liquid-Metal–Amorphous-Semiconductor Transition in Germanium. *Phys. Rev. B* **1994**, *49*, 14251−14269.
(58) Perdew, J. P.; Ernzerhof, M.; Burke, K. Rationale for Mixing Exact Exchange with Density Functional Approximations. *J. Chem. Phys.* **1996**, *105*, 9982−9985.
(59) Perdew, J. P.; Burke, K.; Ernzerhof, M. Generalized Gradient Approximation Made Simple. *Phys. Rev. Lett.* **1996**, *77*, 3865.
(60) Kresse, G.; Joubert, D. From Ultrasoft Pseudopotentials to the Projector Augmented-Wave Method. *Phys. Rev. B* **1999**, *59*, 1758−1775.
(61) Grimme, S. Semiempirical Gga-Type Density Functional Constructed with a Long-Range Dispersion Correction. *J. Comput. Chem.* **2006**, *27*, 1787−1799.
(62) Krukau, A. V.; Vydrov, O. A.; Izmaylov, A. F.; Scuseria, G. E. Influence of the Exchange Screening Parameter on the Performance of Screened Hybrid Functionals. *J. Chem. Phys.* **2006**, *125*, 224106.
(63) Shishkin, M.; Marsman, M.; Kresse, G. Accurate Quasiparticle Spectra from Self-Consistent Gw Calculations with Vertex Corrections. *Phys. Rev. Lett.* **2007**, *99*, 246403.
(64) Rohlfing, M.; Louie, S. G. Electron-Hole Excitations in Semiconductors and Insulators. *Phys. Rev. Lett.* **1998**, *81*, 2312−2315.
(65) Baroni, S.; de Gironcoli, S.; Dal Corso, A.; Giannozzi, P. Phonons and Related Crystal Properties from Density-Functional Perturbation Theory. *Rev. Mod. Phys.* **2001**, *73*, 515−562.
(66) Giannozzi, P.; Andreussi, O.; Brumme, T.; Bunau, O.; Nardelli, M. B.; Calandra, M.; Car, R.; Cavazzoni, C.; Ceresoli, D.; Cococcioni, M.; Colonna, N.; Carnimeo, I.; Dal Corso, A.; de Gironcoli, S.; Delugas, P.; DiStasio, R. A., Jr.; Ferretti, A.; Floris, A.; Fratesi, G.; Fugallo, G.; Gebauer, R.; Gerstmann, U.; Giustino, F.; Gorni, T.; Jia, J.; Kawamura, M.; Ko, H.-Y.; Kokalj, A.; Küçükbenli, E.; Lazzeri, M.; Marsili, M.; Marzari, N.; Mauri, F.; Nguyen, N. L.; Nguyen, H.-V.; Otero-de-la-Roza, A.; Paulatto, L.; Poncé, S.; Rocca, D.; Sabatini, R.; Santra, B.; Schlipf, M.; Seitsonen, A. P.; Smogunov, A.; Timrov, I.; Thonhauser, T.; Umari, P.; Vast, N.; Wu, X.; Baroni, S. Advanced Capabilities for Materials Modelling with Quantum Espresso. *J. Phys.: Condens. Matter* **2017**, *29*, 465901.
(67) Giannozzi, P.; Baroni, S.; Bonini, N.; Calandra, M.; Car, R.; Cavazzoni, C.; Ceresoli, D.; Chiarotti, G. L.; Cococcioni, M.; Dabo, I.; Dal Corso, A.; de Gironcoli, S.; Fabris, S.; Fratesi, G.; Gebauer, R.; Gerstmann, U.; Gougoussis, C.; Kokalj, A.; Lazzeri, M.; Martin-Samos, L.; Marzari, N.; Mauri, F.; Mazzarello, R.; Paolini, S.; Pasquarello, A.; Paulatto, L.; Sbraccia, C.; Scandolo, S.; Sclauzero, G.; Seitsonen, A. P.; Smogunov, A.; Umari, P.; Wentzcovitch, R. M. Quantum Espresso: A Modular and Open-Source Software Project for Quantum Simulations of Materials. *J. Phys.: Condens. Matter* **2009**, *21*, 395502.
(68) Evans, D. J. Computer "Experiment" for Nonlinear Thermodynamics of Couette Flow. *J. Chem. Phys.* **1983**, *78*, 3297−3302.
(69) Hoover, W. G.; Ladd, A. J. C.; Moran, B. High-Strain-Rate Plastic Flow Studied Via Nonequilibrium Molecular Dynamics. *Phys. Rev. Lett.* **1982**, *48*, 1818−1820.

https://doi.org/10.1021/acsomega.1c04680
ACS Omega 2021, 6, 31919−31925